Translational Oncology
www.transonc.com

Volume 7 Number 6 December 2014 pp. 768–779 768

Evaluating treatment response using DW-MRI and DCE-MRI in trastuzumab responsive and resistant HER2-overexpressing human breast cancer xenografts

Jennifer G. Whisenant[*,†,1], Anna G. Sorace[*,†,1], J. Oliver McIntyre[*,†,‡], Hakmook Kang[#], Violeta Sánchez[**], Mary E. Loveless[*] and Thomas E. Yankeelov[*,†,‡,§,¶,]**

*Institute of Imaging Science, Vanderbilt University, 1161 21st Avenue South, Medical Center North, AA-1105, Nashville, TN 37232-2675; †Departments of Radiology and Radiological Sciences, Vanderbilt University, 1161 21st Avenue South, Medical Center North, AA-1105, Nashville, TN 37232-2675; ‡Departments of Cancer Biology, Vanderbilt University, 1161 21st Avenue South, Medical Center North, AA-1105, Nashville, TN 37232-2675; §Departments of Physics, Vanderbilt University, 1161 21st Avenue South, Medical Center North, AA-1105, Nashville, TN 37232-2675; ¶Departments of Biomedical Engineering, Vanderbilt University, 1161 21st Avenue South, Medical Center North, AA-1105, Nashville, TN 37232-2675; #Departments of Biostatistics, Vanderbilt University, 1161 21st Avenue South, Medical Center North, AA-1105, Nashville, TN 37232-2675; **Departments of Breast Cancer Research Program, Vanderbilt-Ingram Cancer Center, Vanderbilt University, 2220 Pierce Avenue, Nashville, TN 37232-2675

Abstract

We report longitudinal diffusion-weighted magnetic resonance imaging (DW-MRI) and dynamic contrast enhanced (DCE)-MRI (7 T) studies designed to identify functional changes, prior to volume changes, in trastuzumab-sensitive and resistant HER2+ breast cancer xenografts. Athymic mice ($N = 33$) were subcutaneously implanted with trastuzumab-sensitive (BT474) or trastuzumab-resistant (HR6) breast cancer cells. Tumor-bearing animals were distributed into four groups: BT474 treated and control, HR6 treated and control. DW- and DCE-MRI were conducted at baseline, day 1, and day 4; trastuzumab (10 mg/kg) or saline was administered at baseline and day 3. Animals were sacrificed on day 4 and tumors resected for histology. Voxel-based DW- and DCE-MRI analyses were performed to generate parametric maps of ADC, K^{trans}, and v_e. On day 1, no differences in tumor size were observed between any of the groups. On day 4, significant differences in tumor size were observed between treated vs. control BT474, treated BT474 vs. treated HR6, and treated vs. control HR6 ($P < .0001$). On day 1, v_e was significantly higher in the BT474 treated group compared to BT474 control ($P = .002$) and HR6 treated ($P = .004$). On day 4, v_e and K^{trans} were significantly higher in the treated BT474 tumors compared to BT474 controls ($P = .0007$, $P = .02$, respectively). A significant decrease in Ki67 staining reinforced response in the BT474 treated group compared to BT474 controls ($P = .02$). This work demonstrated that quantitative MRI biomarkers have the sensitivity to differentiate treatment response in HER2+ tumors prior to changes in tumor size.

Translational Oncology (2014) 7, 768–779

Address all correspondence to: Thomas E. Yankeelov, Ph.D., Institute of Imaging Science, Vanderbilt University Medical Center, 1161 21st Ave. South, MCN AA-1105, Nashville, TN 37232-2675 USA.
E-mail: thomas.yankeelov@vanderbilt.edu
[1] Authors contributed equally to this work.

Received 25 July 2014; Revised 10 September 2014; Accepted 26 September 2014

1936-5233/14
http://dx.doi.org/10.1016/j.tranon.2014.09.011

Introduction

The human epidermal growth factor receptor 2 (HER2) is overexpressed in approximately 25% of all breast cancers [1,2], and is usually indicative of a more aggressive disease and poorer prognosis [2]. Consequently, specific anti-HER2 therapeutics, such as trastuzumab (Herceptin®, Genentech, San Francisco, CA), have been developed that specifically target HER2 and disrupt downstream signaling pathways [3–5]. When administered with traditional chemotherapy, trastuzumab extends overall survival and slows disease progression in patients with HER2-overexpressing breast cancer [6,7]. Despite the observed survival benefits, trastuzumab is effective in only 25% to 50% of this patient population [8,9], and a majority of patients with metastatic breast cancer that initially respond to treatment will eventually progress. Furthermore, approximately 15% of patients that receive trastuzumab in the adjuvant setting will eventually develop metastatic disease [4]. These variable and unpredictable patient outcomes emphasize the need to develop reliable assessments of disease response early during the course of therapy. If a reliable method to assess early response were available, unsuccessful drugs could be replaced with potentially more effective therapy.

The main tumor cell-autonomous mechanism of action of trastuzumab is inhibition of HER2 homodimerization and downstream signaling of the phosphatidylinositol-3 kinase (PI3K) pathway leading to an inhibition of cell-cycle progression and survival [2]; this implies that PI3K regulated processes, e.g., cellular proliferation and apoptosis [10], are potential biomarkers of clinical response to trastuzumab. As a secondary mechanism of action, trastuzumab has been observed to alter tumor microvasculature causing normalization and regression of tumor associated blood vessels and a reduction in vessel diameter, volume, and permeability [11,12]. Additionally, gene expression assays reveal that pro-angiogenic factors, such as vascular endothelial growth factor (VEGF), are downregulated [11,12]. In contrast, the anti-angiogenic factor thrombospondin 1 is upregulated after trastuzumab treatment [11]. Thus, biomarkers reflecting tumor vessel architecture and function may also be useful in assessing early clinical response to trastuzumab.

There are a number of imaging techniques that report on specific characteristics of the tumor microenvironment and response to therapy. Diffusion-weighted magnetic resonance imaging (DW-MRI) is a technique that provides a noninvasive, quantitative characterization of tumor cytoarchitecture [13]. DW-MRI depends on the microscopic, thermally-induced behavior of water molecules moving in a random pattern, referred to as Brownian motion. In a system defined by small compartments (e.g., cellular tissues) that are separated by semi-permeable membranes, the rate of Brownian motion or self-diffusion will be less than that of free diffusion. In cellular tissues, this rate of self-diffusion is described by an apparent diffusion coefficient (ADC), which is influenced by the number, permeability, and separation of barriers that act to restrict the free diffusion of water molecules [14]. DW-MRI data can be used to construct parametric maps of the ADC, and in well-controlled situations, ADC has been shown to correlate inversely with tissue cell density [15]. DW-MRI has been used to assess response to a variety of therapies in both preclinical models [16–18] and clinical studies of breast cancer [19–21].

Dynamic contrast enhanced MRI (DCE-MRI) is an imaging technique that is sensitive to changes in physiological characteristics of tumor microvasculature [22]. DCE-MRI characterizes the pharmacokinetics of an injected contrast agent (CA) as it enters and exits a region of interest (ROI) or tissue. By acquiring serial T_1-weighted images of the MRI signal over time, the kinetics of the CA can be quantified using (for example) a two-compartment model to estimate biologically relevant parameters relating to tumor microvasculature, such as, blood flow, vessel permeability, and tissue volume fractions. These quantitative measurements have been used to assess treatment response in a variety of cancer models and treatment regimens [14,23,24]. More recently, the clinical utility of DCE-MRI to predict responders earlier in the course of therapy (either chemotherapy, radiotherapy or a combination) has been reported in breast cancer [25].

Although DW-MRI and DCE-MRI have been investigated in both preclinical and clinical settings, translation into routine clinical care has been limited. This can be attributed to the inadequate understanding of whether these imaging protocols can predict therapeutic efficacy, as well as the lack of validation (*via* e.g., histological analysis) to assist in the interpretation of the imaging data [13,26]. Thus, the primary objectives of this study were to determine if DW-MRI and DCE-MRI can assess early treatment response (i.e., before changes in tumor size) in trastuzumab-sensitive xenografts. We also explored the sensitivity of DW-MRI and DCE-MRI to differentiate between trastuzumab responsive and resistant HER2-overexpressing xenografts after exposure to treatment. Lastly, we performed immunohistochemistry (IHC) analyses that reflect on cellular proliferation and microvasculature in order to investigate the relationship between the imaging data and the underlying biology. This study provides insight into translational quantitative imaging metrics that have the potential to be applied towards the personalization of HER2 + breast cancer treatment regimens.

Materials and Methods

Cell Lines

Trastuzumab sensitive (BT474) and resistant (HR6) cell lines were generously supplied from the Laboratory of Dr. Carlos Arteaga (Vanderbilt University, Nashville, TN) and cultured in improved minimal essential medium (IMEM, Invitrogen, Carlsbad, CA) supplemented with 10% fetal bovine serum and 1% insulin at 37°C in a humidified, 5% CO_2 incubator. The HR6 cell line was developed *in vivo* from the BT474 cell line as described previously [27]. To maintain trastuzumab resistance, HR6 cells were cultured with 10 μg/ml trastuzumab [27]. Trastuzumab was purchased from the Vanderbilt University Medical Center Outpatient Pharmacy (Nashville, TN). Both cell lines were harvested with trypsin at approximately 85% confluence for inoculation.

Xenograft Models

Female athymic mice ($N = 33$, 4–6 weeks old, Harlan Laboratories, Indianapolis, IN) were implanted with 0.72 mg, 60-day release, 17β-estradiol pellets (Innovative Research of America, Sarasota, FL. Twenty-four hours later, BT474 or HR6 cells (~ 1×10^7) grown to ~85% confluence were suspended in a 100 μL volume with a 1:10 ratio of growth factor-reduced Matrigel and IMEM and were injected subcutaneously into the right flank. Tumor volumes were measured once per week using calipers. A 26-gauge jugular catheter was surgically implanted two days prior to the start of imaging. Mice were anesthetized with 2% isoflurane in pure oxygen mixture for all surgical procedures and imaging. Our institution's Animal Care and Use Committee approved all animal procedures.

Tumors were allowed to grow until they reached ≥200 mm^3, which was typically four to eight weeks post cell inoculation. Mice were grouped into four cohorts: trastuzumab and vehicle treated BT474 cohorts, and trastuzumab and vehicle treated HR6 cohorts. Animals were imaged at three time points: a baseline scan acquired prior to therapy, and then two subsequent imaging sessions at days 1 and 4, which were 24 hours post first and second treatments, respectively. Therapy consisted of two treatments that were administered immediately following imaging at baseline and on day 3. Each treatment included an intra-peritoneal injection (total volume of 100 μL) of trastuzumab (10 mg/kg) or saline vehicle. (A dose of 10 mg/kg was chosen to approximate the clinical dose currently given to breast cancer patients [8,28,29].) Prior to this study, a dose-response analysis was utilized to evaluate and confirm BT474 tumors in response to trastuzumab (10 mg/kg) treatment. With trastuzumab treatment two times per week, treated mice (N = 4) experienced at least 50% regression in tumor size by day 8, while untreated (N = 4) experienced 40% increase in tumor volume [30].

Data Acquisition

All MRI data were collected using a 7 T MRI scanner (Agilent Technologies (formally Varian), Palo Alto, CA) equipped with a 38-mm quadrature RF coil (Doty Scientific, Columbia, SC). Animal respiration rate was monitored, and body temperature was maintained at 37°C by means of a flow of warm air directly into the bore of the magnet. Each animal was placed in a custom built restraint, and the tumor region was first localized *via* 3D gradient echo scout images. T_2-weighted images covering the entire tumor volume were acquired using a fast spin-echo pulse sequence with the following parameters: TR = 5500 ms, effective TE = 35.6 ms, 1 mm slice thickness, and an acquisition matrix of 128 × 128 over a 28 × 28 mm^2 field of view yielding a voxel size of 0.22 × 0.22 × 1 mm^3.

Diffusion-weighted images were acquired using a standard pulsed gradient spin echo sequence with three b values (150, 500, and 800 s/mm^2) and gradients applied simultaneously along three orthogonal directions (x, y, and z). Scan acquisition parameters were: TR/TE = 2000/30 ms, gradient duration δ = 3 ms, gradient interval Δ = 20 ms, two signal excitations, 15 one mm thick slices, and an acquisition matrix of 64 × 64 over a 28 × 28 mm^2 field of view yielding a voxel size of 0.44 × 0.44 × 1 mm^3. Image acquisition was triggered with respiration and navigator corrected [31] to reduce image artifacts due to bulk motion.

After DW-MRI, precontrast T_1 maps were obtained *via* an inversion recovery fast low angle shot gradient echo sequence with an adiabatic inversion pulse and seven inversion times: 0.25, 0.45, 0.83, 1.5, 2.7, 5.0, and 10 seconds. The imaging parameters were as follows: $TR/TE/\alpha$ = 12,000 ms/2.1 ms/15°, NEX = 2, 15 one mm thick slices, an acquisition matrix of 64 × 64, and a 28 × 28 mm^2 FOV yielding a voxel size of 0.44 × 0.44 × 1 mm^3. Dynamic T_1-weighted images were acquired using a spoiled gradient echo sequence at a temporal resolution of 12.8 seconds for 20 minutes with the following parameters: $TR/TE/\alpha$ = 100 ms/2.1 ms/25°, NEX = 2, and the same acquisition matrix and FOV as the precontrast T_1 map. A bolus of 0.05 mmol/kg Gd-DTPA was delivered *via* a jugular catheter using an automated syringe pump (Harvard Apparatus, Holliston, MA) at a rate of 2.4 mL/min after 2 minutes of baseline images were acquired.

Data Analysis

ADC parametric maps were constructed by fitting the MR signal intensities from images acquired at three b values using a nonlinear least squares optimization method to Eq. (1):

$$S(b) = S_0 \cdot e^{-ADC \cdot b}, \tag{1}$$

where S_0 and $S(b)$ are the signal intensities before and after application of the diffusion gradients, respectively. The median ADC was quantified from the whole tumor volume. If the ADC of the water phantom was greater than ± 15% of free water at 37°C [32], then the corresponding tumor ADC slice was removed from the DW-MRI analysis. All DW-MRI data analysis methods were performed in MATLAB® (version R2013b; The MathWorks, Natick, MA). Voxels were removed from the DW-MRI analysis if the fitting route yielded an ADC value less than zero or greater than 3×10^{-3} mm^2/sec.

Data collected for the T_1 map were fit for every image voxel using a nonlinear least squares method to the following equation:

$$S = \left| S_0 \cdot \left(1\text{-}2 \cdot e^{-TI/T_1}\right) \right|, \tag{2}$$

where S_0 and S are the signal intensities at thermal equilibrium and inversion time, respectively, and TI is the inversion time. Once T_1 maps were calculated, signal intensity time courses from all tumor voxels were fit to the standard two-compartment Tofts-Kety model to extract pharmacokinetic parameters [33,34] which is given by Eq. (3):

$$C_t(t) = K^{trans} \int_0^t C_p(u) \cdot e^{-\left(K^{trans}/v_e\right)(tu)}\, du, \tag{3}$$

where C_t and C_p are the concentrations of the contrast agent in the tissue and plasma compartment, respectively, K^{trans} is the volume transfer constant between C_p and C_t, and v_e is the extravascular extracellular volume fraction.

The signal intensity time courses from each voxel were fit to Eq. (3) using a nonlinear least squares approach by incorporating: 1) the precontrast T_1 value, 2) the fast exchange limit model [22] with relaxivity for gadopentetate at 7 T, r_1 = 4.72 mM^{-1} s^{-1} [35], and 3) a population-derived vascular input function collected from a cohort of 10 athymic female mice using the identical protocol described by Loveless et al. [35]. Additionally, the population-derived vascular input function was individualized for each animal in the current study using the method previously described [36]. Briefly, a ROI was drawn across three slices in the muscle to generate an averaged signal intensity time course. This time course was then fit to the two-compartment model in an iterative fashion until the v_e of the muscle equaled a physiologically relevant value (i.e., 0.11) [37]. Voxels were removed from the DCE-MRI analysis if the fitting routine yielded a K^{trans} value less than 0.01 min^{-1} or greater than 5 min^{-1}, and a v_e value greater than 1.

Histological Analysis

All animals were sacrificed after the final imaging time point on day 4 and tumors were excised. Tumors were placed in tissue cassettes and fixed in 10% formalin, before being stored in 70% ethanol. Serial sections of tumor (5 μm thick) were cut from the central slices of paraffin-embedded tissue blocks and floated onto charged glass slides and dried overnight. A hematoxylin and eosin (H&E) stained section was obtained from the tissue block. Following antigen retrieval on the

remaining sections, the tissue sections were stained with anti-CD31 (ab28364, Abcam Cambridge, MA) or anti-Ki67 (M7240, Dako Carpinteria, CA). Slides were digitally scanned in high resolution (20×) brightfield with a Leica (Leica Microsystems Inc, Ariol, Buffalo Grove, IL) SCN400 Slide Scanner. H&E sections were examined for cellular necrosis and reported as a percentage of tumor cross-sectional area. Necrotic tissue within the tumor was manually segmented, and percent necrosis was reported as the ratio of the segmented area to total tumor area (Image J, Softonic, San Francisco, CA). The associated software with the Leica SCN400 package was utilized for unbiased, automated image analysis and quantification of immunostaining in brightfield. Using H&E sections, four regions of viable tissue were selected (total area = 1.53 mm^2); the four regions were applied to the corresponding Ki67 and CD31 slides using a linking tool to ensure comparable regions of tissue were analyzed for all histology quantification. The program was trained to select microvessel, proliferation, and nuclei based on coloring and size. Microvessel density was examined through analysis of total microvessels per area through CD31 staining. Cellular density was calculated as the total number of nuclei per square millimeter detected within the four viable regions of tissue on the H&E stained sections. Cell proliferation (Ki67 staining) was calculated as the percentage of proliferating nuclei per total nuclei detected within the four viable tissue regions on the Ki67 stained sections of tumor.

Statistical Analysis

To assess group changes in tumor volume, ROIs were manually drawn along tumor boundaries obtained from the high resolution anatomical MR images from all slices consisting of tumor tissue. The same ROIs were copied to the DW-MRI and DCE-MRI data, and the median ADC, K^{trans}, and v_e were quantified from the tumor ROIs.

The analysis of variance repeated measures with Sidak test to correct for multiple comparisons was used to compare: 1) trastuzumab versus vehicle BT474, 2) treated BT474 versus treated HR6, and 3) trastuzumab versus vehicle treated HR6 cohorts. Statistical analysis was only performed on the percent change data using GraphPad Prism version 6.00 for Windows (GraphPad Software Inc., La Jolla, CA). Differences in the immunohistological data and tumor volume were also tested for significance using analysis of variance repeated measures with Sidak test to correct for multiple comparisons; $P < .05$ was taken as the significance threshold. All data are presented as mean ± standard error of the mean (SEM).

Results

The percent change in tumor volumes at each imaging time point are displayed for each cohort in Figure 1; absolute values and percent change from baseline are presented for each group and time point in Table 1. The number of mice for each cohort and time point is displayed for each imaging parameter in Tables 2 to 4. Longitudinal percent changes in tumor volume for the treated and control BT474 tumors are displayed on Figure 1*A*; significant differences in changes in tumor volume between these groups were not observed at baseline or day 1 ($P > .05$), but were significantly different at day 4 ($P < .0001$). Percent change in tumor volume at each time point is displayed in Figure 1*B* for the treated BT474 and treated HR6 tumors. Significant differences between changes in tumor volume in these cohorts were not observed at baseline or day 1 ($P > .05$), but were significant at day 4 ($P < .0001$). Lastly, longitudinal percent changes in tumor volume for the treated and control HR6 tumors are displayed in Figure 1*C*; a significant difference in changes in tumor volume was not observed at baseline or day 1 ($P > .05$), but a significant difference was observed on day 4 ($P < .0001$).

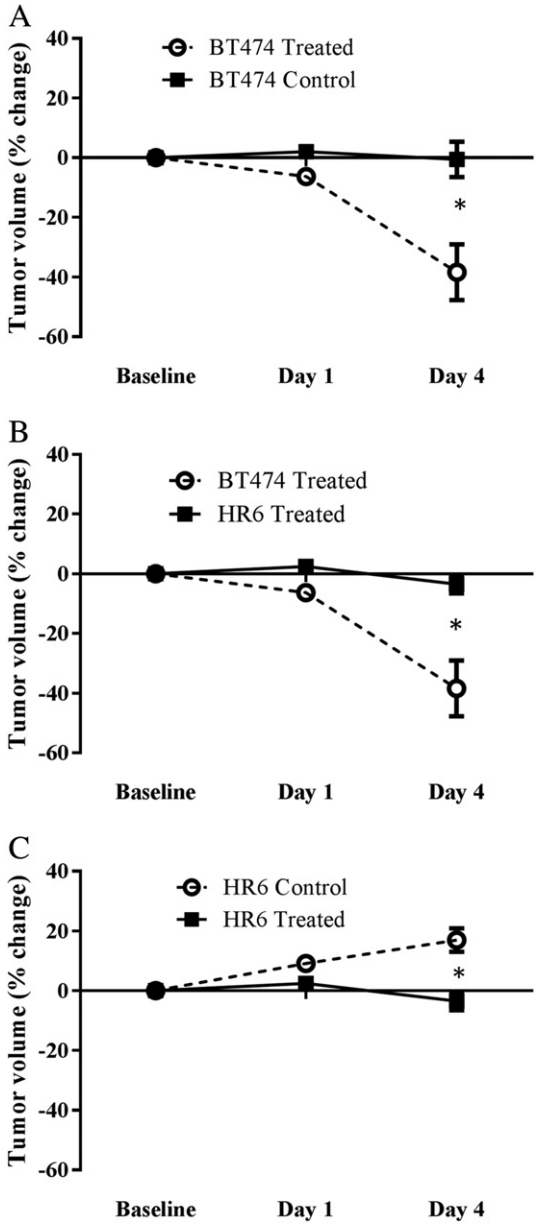

Figure 1. Tumor volume changes are shown for the following comparisons: (A) BT474 Treated vs. BT474 Control, (B) BT474 Treated vs. HR6 Treated, and (C) HR6 Treated vs. HR6 Control. There are no significant differences in tumor volumes between any of the cohort comparisons on day 1 ($P > .05$). Percent change in tumor volume is significantly lower in the treated BT474 cohort compared to both the BT474 controls ($P < .0001$) and the HR6 treated ($P < .0001$) animals on day 4. Additionally, tumor volume is significantly higher in the HR6 control compared to HR6 treated tumors ($P < .0001$) on day 4. *$P < .05$.

DW-MRI Analysis

ADC maps were constructed and are displayed in Figure 2 as overlays on T_2-weighted anatomical images; absolute ADC values

Table 1. Tumor Volume (and Percent Change +/− SEM from Baseline) for Each Group on Baseline, day 1, and day 4

Animal Cohort	Baseline ($\times 10^{-4}$ mm^2/s)	Day 1 ($\times 10^{-4}$ mm^2/s)	Day 4 ($\times 10^{-4}$ mm^2/s)
BT474 treated	232 ± 29	219 ± 27 (*−6.31 ± 2.11%*)	145 ± 28 (*−38.3 ± 7.14%*)
HR6 treated	296 ± 45	302 ± 46 (*2.42 ± 1.56%*)	289 ± 48 (*−3.47 ± 2.48%*)
BT474 control	200 ± 38	227 ± 35 (*2.02 ± 1.62%*)	229 ± 45 (*−0.57 ± 5.13%*)
HR6 control	376 ± 39	411 ± 43 (*9.10 ± 1.62%*)	445 ± 52 (*17.0 ± 3.70%*)

Table 3. Average K^{trans} Values (and Percent Change +/- SEM from Baseline) for Each Group on Baseline, day 1, and day 4

Treatment Group	Baseline (min^{-1})	Day 1 (min^{-1})	Day 4 (min^{-1})
BT474 treated	0.19 ± 0.02 (*N = 12*)	0.22 ± 0.03 (*N = 12*) (*14.57 ± 12.91%*)	0.31 ± 0.03 (*N = 7*) (*53.53 ± 11.63%*)
HR6 treated	0.14 ± 0.02 (*N = 5*)	0.10 ± 0.01 (*N = 5*) (*−25.39 ± 9.17%*)	0.19 ± 0.04 (*N = 5*) (*38.93 ± 26.77%*)
BT474 control	0.18 ± 0.04 (*N = 8*)	0.17 ± 0.02 (*N = 7*) (*12.35 ± 24.17%*)	0.14 ± 0.02 (*N = 6*) (*−12.68 ± 21.15%*)
HR6 control	0.13 ± 0.02 (*N = 6*)	0.11 ± 0.01 (*N = 6*) (*3.58 ± 16.67%*)	0.14 ± 0.02 (*N = 5*) (*33.32 ± 21.02%*)

and percent change from baseline (mean ± SEM) are presented for each group and imaging time point in Table 2. One representative animal from each cohort is displayed in each of four rows (BT474 treated, HR6 treated, BT474 control, and HR6 control, respectively), whereas each column represents an imaging time point (baseline, day 1, and day 4, respectively). Qualitatively, the ADC parametric maps show little change in the BT474 treated and control groups, and an increase over time in both HR6 cohorts.

Comparison of the ADC data between the BT474 treated and control groups, as seen in Figure 3*A*, demonstrated no significant differences at any time point during the study ($P > .05$). There were no significant differences between the BT474 treated and HR6 treated cohorts on day 1 ($P = .61$). On Day 4, however, ADC was significantly higher ($P = .003$) in the HR6 treated group, as seen in Figure 3*B*. Comparison of the treated and control nonresponder HR6 groups, as seen in Figure 3*C*, revealed no significant differences between the groups on any of the days ($P > .05$).

DCE-MRI Analysis

Parametric maps of K^{trans} and v_e were constructed and overlaid on T_2-weighted anatomical images, and are displayed in Figure 4*A* and *B*, respectively. Similarly to the DW-MRI data, one representative animal from each cohort is displayed in each of four rows of Figure 4, while the columns represent the different imaging time points. Qualitatively, these maps illustrate a longitudinal increase in K^{trans} for the treated BT474 cohort and a decrease in the BT474 controls. K^{trans} appears to increase over the imaging time points in the treated HR6 animal, while remaining relatively unchanged in the control HR6 animal.

The parametric maps of v_e reveal longitudinal increases in the BT474 treated groups, while their control cohorts show relatively no changes. However, the parametric maps of the treated and control HR6 cohorts reveal a longitudinal increase in v_e, as well as large regions that contain voxels with physiologically implausible values (i.e., $v_e > 1$), which is probably due to an increase in necrosis. These voxels are set to zero and removed from the quantitative DCE-MRI analysis.

The absolute values and percent change from baseline (mean ± SEM) are presented for each group and imaging time point in Tables 3 and 4 for K^{trans} and v_e, respectively. The percent change in K^{trans} was not significantly different between treated and control BT474 cohorts on day 1 (Figure 5*A*; $P = .99$). However, on day 4, K^{trans} was significantly elevated in the treated BT474 tumors compared to their control counterparts (Figure 5*A*; $P = .02$). K^{trans} was not significantly different at day 1 or day 4 between the treated BT474 and HR6 cohorts (Figure 5*B*; $P > .05$). Additionally, no significant differences in K^{trans} were observed between treated and control HR6 tumors at any time point during the study (Figure 5*C*; $P > .05$).

The v_e of the treated BT474 cohort was significantly higher on day 1 (Figure 5*D*; $P = .002$) and day 4 (Figure 5*D*; $P = .0007$) compared to BT474 controls, revealing an early response detected by imaging prior to changes in tumor size. Additionally, v_e was significantly higher on day 1 in the treated BT474 compared to the treated HR6 cohort (Figure 5*E*; P = 0.004) though it was not significantly different at day 4 (Figure 5*E*; $P = .61$). The v_e values in the HR6 treated group were not significantly different compared to their control counterparts at any time point (Figure 5*F*; $P > .05$).

Histological Analysis

Histological analysis was performed on tissue obtained at day 4 after the final imaging time point. Representative images of H&E, Ki67, and CD31 are shown in Figure 6. A qualitative assessment of histology stains shows that the BT474 treated group has less cells undergoing proliferation (Ki67 stain; Figure 6, panel *B*) compared to the other three groups (Figure 6, *E*, *H*, and *K*). Also, the treated BT474 and HR6 groups appear to have more microvessels (CD31 stain; Figure 6, *C* and *I*) in comparison to their untreated counterparts (Figure 6, *F* and *L*). It is also interesting that the HR6 tumors (both treated and control) appear to

Table 2. Average ADC Values (and Percent Change +/− SEM from Baseline) for Each Treatment Group on Baseline, day 1, and day 4

Animal Cohort	Baseline ($\times 10^{-4}$ mm^2/s)	Day 1 ($\times 10^{-4}$ mm^2/s)	Day 4 ($\times 10^{-4}$ mm^2/s)
BT474 treated	6.90 ± 0.30 (*N = 11*)	7.59 ± 0.40 (*N = 10*) (*8.86 ± 10.30%*)	8.06 ± 0.35 (*N = 8*) (*15.52 ± 22.59%*)
HR6 treated	6.18 ± 0.36 (*N = 5*)	7.42 ± 0.39 (*N = 5*) (*21.48 ± 5.04%*)	9.80 ± 0.71 (*N = 4*) (*56.85 ± 15.91%*)
BT474 control	6.44 ± 0.26 (*N = 8*)	7.10 ± 0.49 (*N = 6*) (*14.91 ± 14.33%*)	6.75 ± 0.58 (*N = 5*) (*11.94 ± 14.66%*)
HR6 control	7.29 ± 0.66 (*N = 7*)	6.96 ± 0.40 (*N = 7*) (*0.29 ± 9.91%*)	8.09 ± 0.30 (*N = 5*) (*27.89 ± 22.28%*)

Table 4. Average v_e Values (and Percent Change +/- SEM from Baseline) for Each Group on Baseline, day 1, and day 4

Treatment Group	Baseline	Day 1	Day 4
BT474 treated	0.27 ± 0.03 (*N = 12*)	0.38 ± 0.04 (*N = 12*) (*54.73 ± 12.91%*)	0.47 ± 0.04 (*N = 7*) (*71.77 ± 14.84%*)
HR6 treated	0.35 ± 0.01 (*N = 5*)	0.31 ± 0.04 (*N = 5*) (*−12.02 ± 9.11%*)	0.51 ± 0.04 (*N = 5*) (*47.78 ± 13.40%*)
BT474 control	0.29 ± 0.03 (*N = 8*)	0.29 ± 0.03 (*N = 7*) (*−2.10 ± 10.57%*)	0.29 ± 0.03 (*N = 6*) (*−2.67 ± 11.70%*)
HR6 control	0.28 ± 0.06 (*N = 6*)	0.31 ± 0.03 (*N = 6*) (*21.86 ± 13.60%*)	0.36 ± 0.03 (*N = 5*) (*53.07 ± 38.43%*)

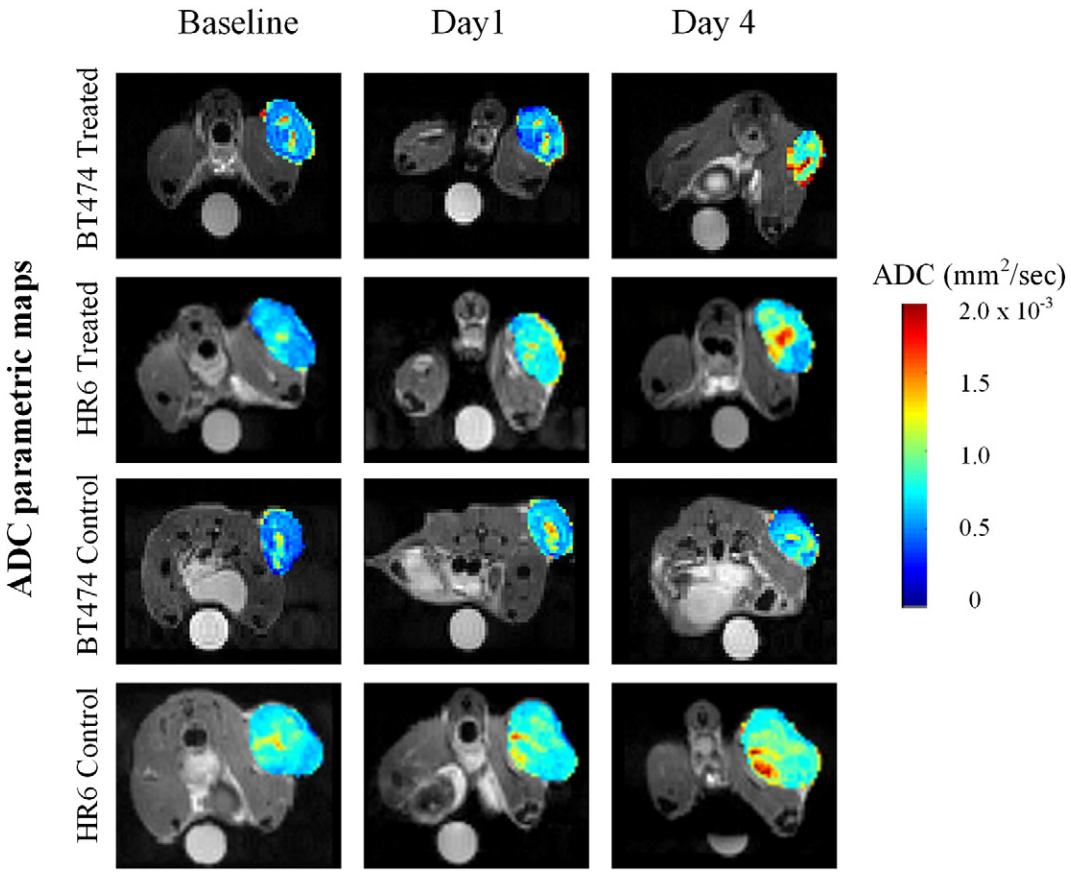

Figure 2. DW-MRI ADC parametric maps of a representative mouse from each cohort. The columns indicate baseline, day 1, and day 4 time points whereas each row indicates each of the four groups. Regions with noticeably increased ADC values are observed within the center of the treated and control HR6 cohorts, indicating possible areas of cell death (necrosis).

have less cell density (as visualized in the H&E stain; Figure 6, *G* and *J*) compared to both BT474 cohorts.

Visual assessment of overall cell density, percent proliferation, and microvessel density (Figure 6) are consistent with the quantitative assessment shown in Figure 7. Comparing the BT474 treated and control cohorts, there were no significant differences in cell density ($P > .99$, Figure 7*A*) or necrosis ($P = .98$, Figure 7*B*). Furthermore, HR6 treated and control groups also exhibited no significant differences in cell density ($P = .99$, Figure 7*A*) or necrosis ($P > .99$, Figure 7*B*). Interestingly, there is less (−48.3%) cell density in the HR6 control group as compared to the BT474 control group ($P = .10$). There is also a higher, yet not significant, percent necrosis ($P = 0.71$) in the HR6 control tumors compared to the BT474 control groups. Ki67 analysis showed significantly less proliferation in the BT474 treated tumors compared to BT474 control (Figure 7*C*, $P = .05$). Additionally, the difference in Ki67 staining between BT474 treated and HR6 treated was significantly different ($P = .005$, Figure 7*C*), with the HR6 treated group demonstrating 52.4% proliferation compared to 18.7% in the BT474 treated. There were no significant proliferation differences between HR6 treated and control tumors ($P = .40$, Figure 7*C*). BT474 treated and HR6 treated tumors reveal a slightly greater, yet not significant, microvessel density (microvessels per area) compared to their control counterparts ($P = .84$ and $P = .32$, respectively), as seen in Figure 7*D*.

Discussion

The main mechanism of action of trastuzumab appears to be the disruption of downstream cell signaling pathways leading to inhibition of cellular proliferation and survival [2,4]. A secondary mechanism of action has been observed where trastuzumab acts as an anti-angiogenic agent to reduce vascular volume and flow [11]. The former observation will necessarily occur earlier than changes in tumor size. Additionally, treatment-induced changes in tumor vasculature might also occur prior to changes in tumor morphology. A unique advantage of imaging tumor physiology is that quantitative functional and molecular imaging techniques have the ability to capture treatment-induced changes before any volumetric changes in tumor growth are observed, thereby providing an early response assessment. Thus, the goal of this study was to examine the sensitivity of DW-MRI and DCE-MRI to the anti-tumor and anti-angiogenic effect of trastuzumab on xenograft models that are sensitive (BT474) and resistant (HR6) to trastuzumab.

As they are defined, the ADC and DCE-MRI pharmacokinetic parameter v_e reflect changes in tumor cytoarchitecture and cell density; therefore, we hypothesized that the ADC and v_e would reflect the anti-proliferative effect of trastuzumab. A quantitative analysis of the DCE-MRI data revealed a significantly higher v_e on day 1 in the BT474 treated group compared to its control counterpart (Figure 5*D*; BT474 control) and its resistant counterpart (Figure 5*E*; HR6). This

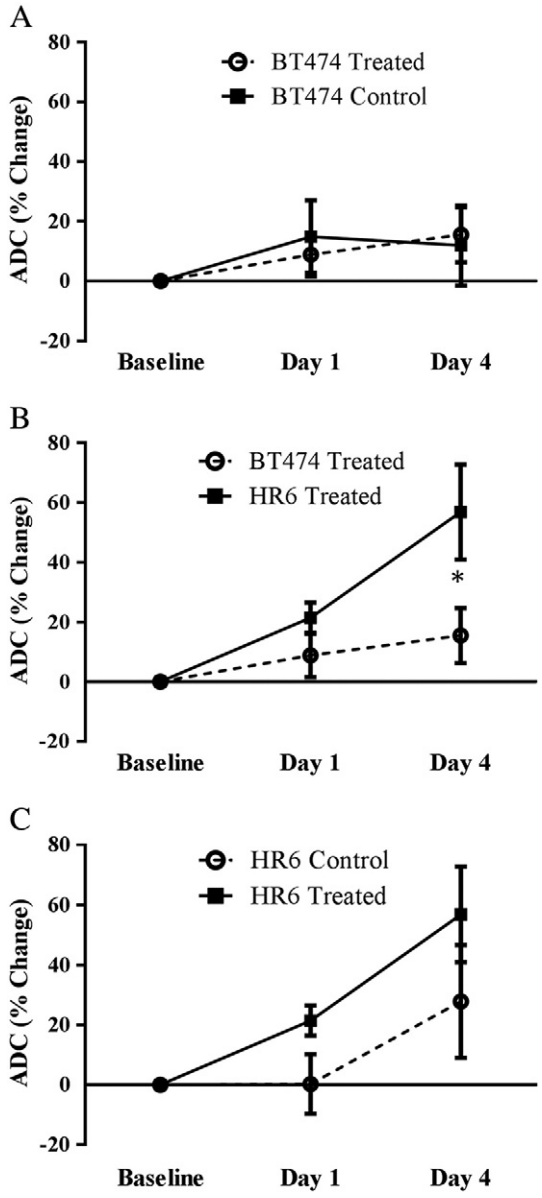

Figure 3. Percent change in ADC measurements are shown for the following comparisons: (A) BT474 Treated vs. BT474 Control, (B) BT474 Treated vs. HR6 Treated, and (C) HR6 Treated vs. HR6 Control. No significant differences in ADC are observed at any time point between the BT474 cohorts ($P > .05$). ADC is significantly higher in the HR6 treated tumors as compared to the BT474 treated tumors on day 4 ($P = .004$). Although no significant differences in ADC were observed between the HR6 cohorts, ADC increased longitudinally in both cohorts. *$P < .05$.

observation is of note as it occurred prior to detection of changes in tumor size that occurred on day 4 (Figure 1*A* and *B*). Significant differences in ADC were not observed between the treated and control BT474 cohorts (Figure 3*A*). This result is not unique, as Aliu et al. did not observe significant changes in the ADC values of BT474 mice at 4 days post gefitinib treatment [18]. However, there are studies that have used ADC to accurately separate treated from control cohorts in preclinical models of basil-like breast cancer [17]; however, these significant changes in ADC were observed at later time points (day 7) after therapy.

Interestingly, the trastuzumab-resistant cohort that received therapy (i.e., treated HR6) exhibited a significantly higher ADC at day 4 ($P = 0.004$) compared to the BT474 treated group (Figure 3*B*). Furthermore, the ADC values in both the HR6 cohorts showed similar increasing longitudinal trends, although they were not significantly different from each other. We hypothesize the increase in ADC is due to a less cell density and greater percent necrosis, which was confirmed from the histological data (Figure 7*A* and *B*). Additionally, observational differences in the ADC and v_e were noticed when comparing the non-treated cohorts; i.e., BT474 control versus HR6 control (this comparison was not statistically compared) (Tables 1 and 3). Less cell density and more necrosis would allow for an increase in water diffusion (ADC) and extravascular extracellular volume fraction (v_e), which are reflective of the differences within each tumor type. Moreover, the quantitative analysis of ADC included the entire tumor (did not exclude a necrotic core), as there are currently no validated or consistently utilized methods to reliably isolate necrotic tissue in subcutaneous tumors, although different approaches have been explored [18,38]. Additionally, it is not currently possible to differentiate between necrosis that developed from the xenograft tumors outgrowing their blood supply and necrosis resulting in response to trastuzumab treatment.

Ki67 staining followed the hypothesized trends as only the trastuzumab-sensitive treated group (i.e., treated BT474) revealed a significantly lower amount of Ki67 staining, which equated to less than 20% of the cells undergoing proliferation (Figure 7*C*). The BT474 control, HR6 treated, and HR6 control groups demonstrated over 40% of the total cells undergoing proliferation. The Ki67 histological results confirm treatment response revealing that trastuzumab is significantly affecting the cellular proliferation in the BT474 trastuzumab-sensitive model, and that the trastuzumab-resistant groups appear to be resistant.

To investigate the sensitivity of DCE-MRI to the anti-angiogenic effect of trastuzumab, we evaluated the longitudinal trends of the pharmacokinetic parameter K^{trans}, which provides a measurement of tumor microvascular flow and permeability. We hypothesized that K^{trans} would decrease in response to effective treatment. However, the opposite was observed as K^{trans} was significantly larger in the trastuzumab-responsive treated group (i.e., BT474 treated) compared to controls (Figure 5*A*). The microvessel density quantified from CD31 staining was larger, yet not significant, in the BT474 treated group (Figure 7*D*), which corresponded with the imaging data. These two results were interesting and unexpected considering previous studies observed a potential decrease in vascularity [11,12]. We hypothesize that these changes in K^{trans} and CD31 microvessel density links trastuzumab therapy to altering vascular function (i.e., perfusion and permeability), and could possibly be utilized to improve the delivery of (for example) cytotoxic therapy in the future [39,40]; this is the subject of an ongoing investigation in our lab [40].

Trastuzumab has been previously identified as having anti-angiogenic affects in general, and vascular normalization in particular [11]. Vascular normalization is the process of utilizing anti-angiogenic agents to transiently stabilize the abnormal tumor vasculature through balancing the pro- and anti-angiogenic factors. In turn, this creates a more normal vascular phenotype to temporarily improve intratumoral drug delivery. Izumi et al. showed that trastuzumab causes blood vessels within the HER2+ tumor (MDA-MB-361 breast cancer cells derived from brain metastasis implanted grown in cranial windows) to more closely resemble a normal phenotype [11]; a significant reduction in both the diameter of the vessels and the vascular permeability was shown by day 15 (tumors were treated with trastuzumab every three days with 30 mg/kg). Vessel

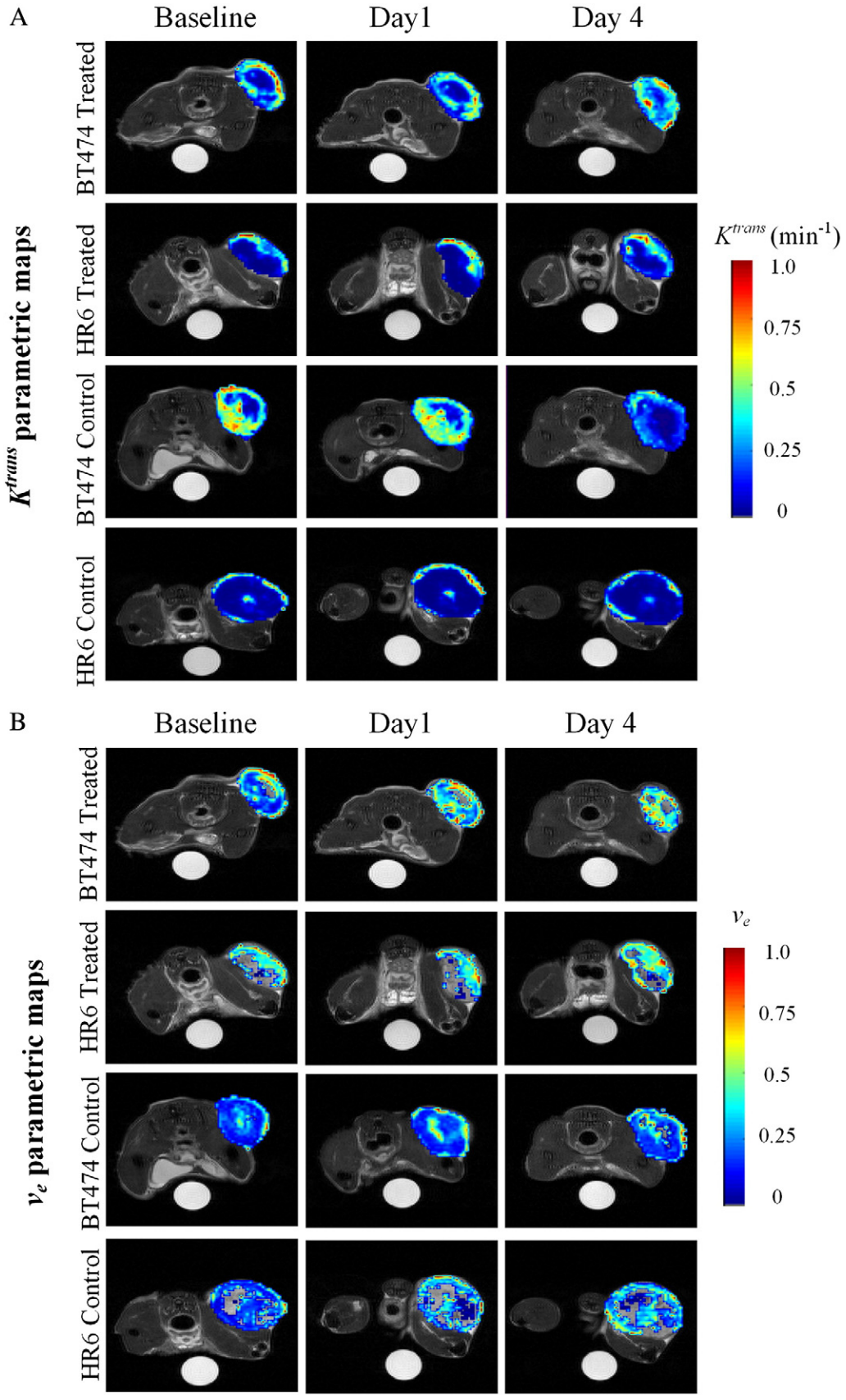

Figure 4. DCE-MRI parametric maps, (A) K^{trans} and (B) v_e, of a representative mouse from each group. The columns indicate baseline, day 1, and day 4 time points whereas each row indicates each of the four groups. K^{trans} parametric maps reveal enhancement along the periphery with increasing trends in the BT474 treated group. K^{trans} parametric maps remain fairly consistent in HR6 treated groups, while the BT474 control and HR6 control groups slightly decrease over time. v_e parametric maps reveal variations within all the observed tumors, with increased levels in the treated groups compared to controls.

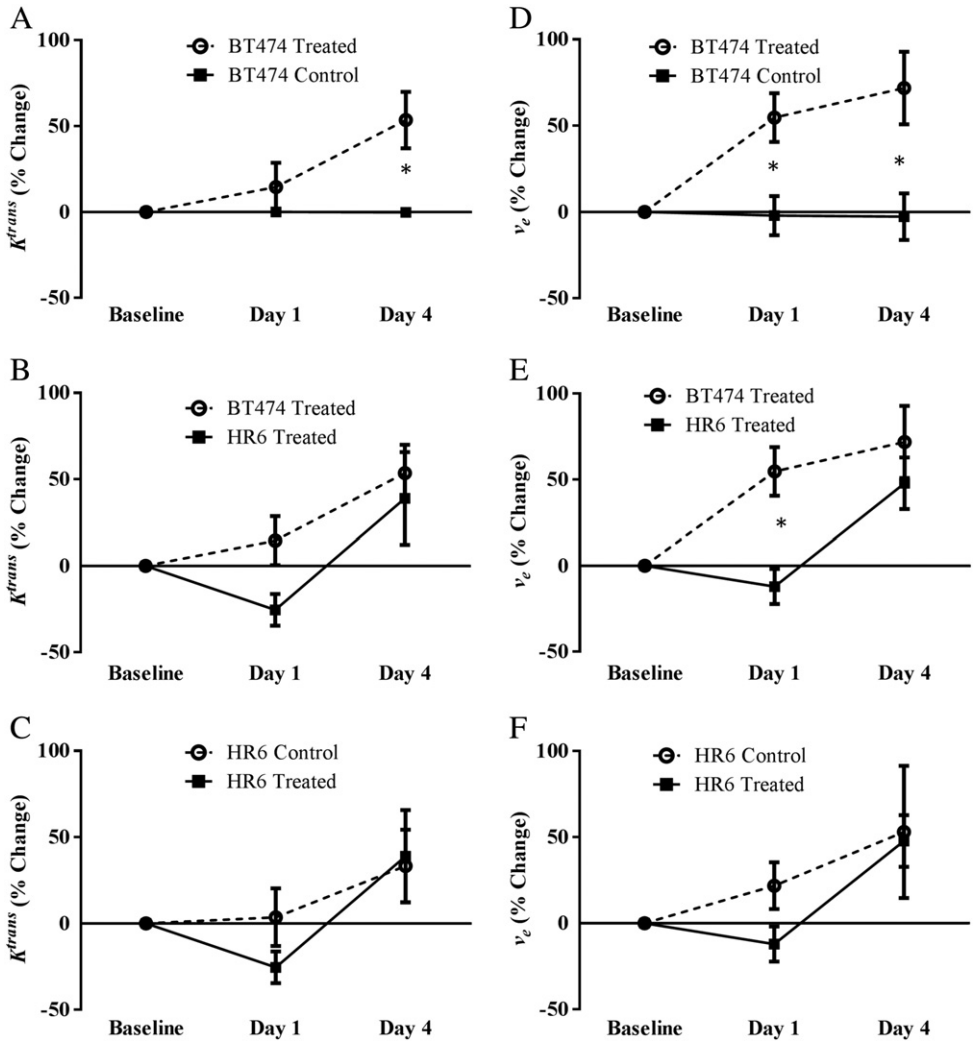

Figure 5. DCE-MRI parameters, K^{trans} and v_e, reveal significant differences between the animal groups. Shown are comparisons between (A, D) BT474 Treated vs. BT474 Control, (B, E) BT474 Treated vs. HR6 Treated, and (C, F) HR6 Treated vs. HR6 Control. v_e is significantly higher in the BT474 treated group compared to both the BT474 control and the HR6 treated groups on day 1 ($P = .002$, $P = .004$, respectively). Both K^{trans} and v_e reveal increasing trends in the BT474 treated group compared to its control counterpart on day 4 ($P = .02$, $P = .007$, respectively). No significant differences in either of the DCE-MRI parameters were observed between the HR6 treated and control groups. *$P < .05$.

diameter and volume was 2.8-fold and 6.6-fold less in the trastuzumab treated tumors compared to control tumors, while trastuzumab also increased survival by 65% compared to controls. To investigate these anti-angiogenic effects, angiogenesis-related genes were investigated; trastzumab-treated tumors revealed lower levels of VEGF, TGF-α, Ang-1, PAI-1, and higher levels of TSP-1 compared to control tumors [11,41]. A study by Heyerdahl et al. analyzed changes in DCE-MRI parameters after ^{227}Th-trastuzumab radiotherapy in xenograft tumors [42]. Although radiotherapy has the potential to increase permeability and damage vasculature, the tumors treated with trastuzumab labeled ^{227}Th were well perfused and exhibited vascular stability [42]. This study also revealed a significant increase in k_{ep} ($=K^{trans}/v_e$; the rate of contrast wash-out from extracellular space to plasma) compared to control tumors on week two and three. This more normal phenotype in a tumor could potentially be indicating vascular normalization. These previous studies in combination with our data indicate that further, prospective, studies on trastuzumab-induced normalization is of interest; a study on this topic is currently underway in our laboratory [40].

Voxels which returned physiologically implausible values form the DCE-MRI analysis (i.e., $v_e > 1$) were removed from the statistical analysis. A possible source of this issue is that the contrast agent is being delivered *via* a diffusion mechanism rather than perfusion, which is the case in completely necrotic tissues or cystic fluid. Thus, this study is limited by the accuracy of the Tofts-Kety model in regions of tissue where there is no active perfusion since this model does not account for diffusion. Although there are initial efforts at developing new models that account for contrast agent diffusion [43,44], the Tofts-Kety equation is still the most common method for the quantitative analysis of DCE-MRI data.

Another limitation of the longitudinal study design prevented biological validation at each imaging time point (histology was only taken at day 4); however, this was necessary to quantify longitudinal changes in imaging biomarkers. Follow-up studies will directly match histological samples with each particular imaging time point throughout the study. Accurately characterizing the hypothesized window's opening and closing would allow for optimization of

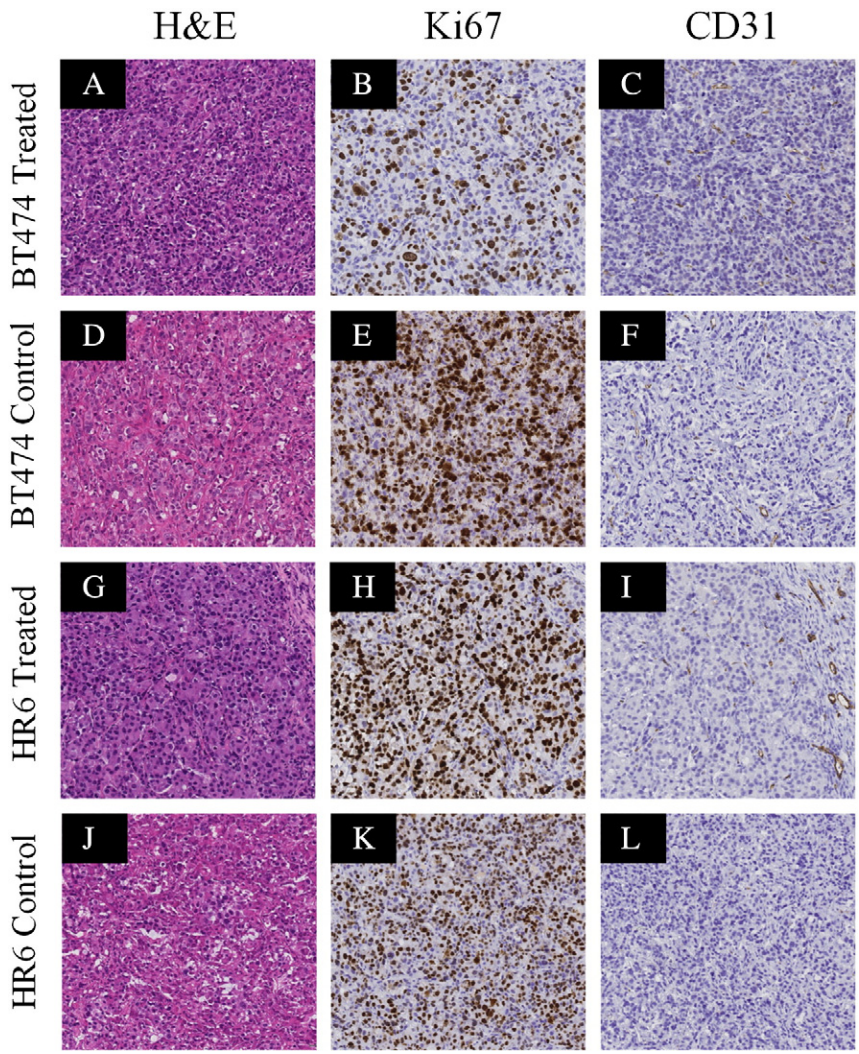

Figure 6. Sample staining (at 20× magnification) for H&E (first column), Ki67 (second column), and CD31 (third column) are shown for BT474 treated (row one), BT474 control (row two), HR6 treated (row three), and HR6 control (row four). Representative images reveal that BT474 tumors (treated and control) exhibit increased cell density compared to the HR6 tumors (treated: panels A and G and control: panels D & J). Additionally, these images reveal decreased proliferation (panel B) in the BT474 treated cohort compared to the BT474 controls (panel E).

treatment regimens and improvement of concomitant drug deliveries, therefore enhancing drug efficiency without increasing dosage. Thus, important data related to the dynamic and transient nature of the imaging parameters may have been missed in the current study. Again, experiments are ongoing to address this issue.

Conclusions

The goal of this study was to evaluate the ability of DW-MRI and DCE-MRI to measure the anti-proliferative and anti-vascular effects of trastuzumab before changes in tumor size became evident in responsive and resistant HER2+ breast cancer xenograft models. As hypothesized, v_e values were significantly greater at day 1 and day 4 in response to treatment in the trastuzumab-responsive xenografts compared to controls ($P < .05$). The significant difference observed on day 1 preceded significant changes in tumor volume that occurred at day 4; therefore, v_e was an early marker of response in trastuzumab-responsive xenografts. These imaging results on day 4 were supported by histology. Additionally, v_e was significantly higher in the BT474 treated group compared to the HR6 treated group at day 1, which again preceded tumor volume changes. Thus, v_e is an early imaging biomarker of response to treatment between xenografts with different trastuzumab sensitivities. Although the heightened values in ADC and v_e within the treated and control trastuzumab-resistant groups were unexpected, histological analysis showed a (non-significant) lower cell density and higher percent necrosis when compared to the trastuzumab-responsive counterparts. The DCE-MRI pharmacokinetic parameter K^{trans} differentiated the treated and control BT474 xenografts; however, the significantly ($P = .02$) higher K^{trans} observed in response to trastuzumab was unexpected and hypothesized to be related to vascular normalization. If proven true, this has opportunity for real clinical impact as the development of imaging methods that can non-invasively identify an optimum window of when to administer, for example, chemotherapy would greatly benefit patient care.

Acknowledgments

We thank the National Institutes of Health for funding through R01 CA138599, R01 CA80195, P50 CA98131, P30 CA68485, U24

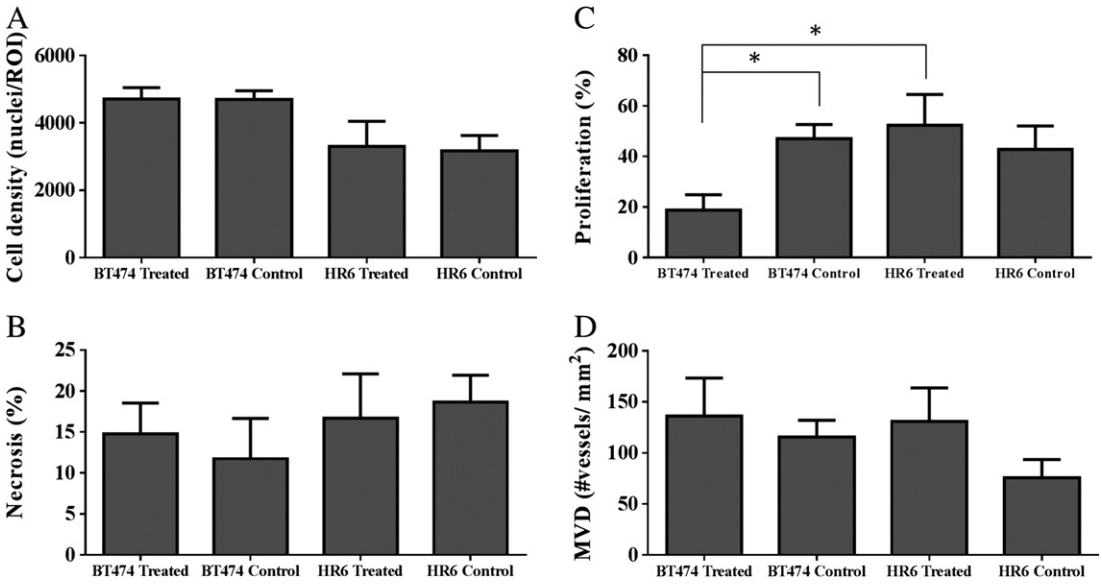

Figure 7. A quantitative analysis of the immunohistochemistry data from day 4 are shown for (A) cell density, (B) percent necrosis, (C) percent Ki67 proliferation expression, and (D) microvessel density. The HR6 treated and control group have less cell density (panel A), or fewer cells per area, in comparison to the BT474 treated and control groups. Additionally, the lower cell density observed in the HR6 cohorts is correlated with a higher percent necrosis (panel B). BT474 treated tumors responded to trastuzumab treatment as a significantly lower proliferation percentage occurred in this cohort as compared to the BT474 controls (panel C). The HR6 treated tumors had a significantly higher proliferation percentage as compared to the treated BT474 cohort ($P = .005$). The CD31 analysis (panel D) shows slightly increasing microvessel density in the treated BT474 and HR6 cohorts in comparison to their control counterparts; however, differences are not statistically significant. *$P < .05$.

CA126588, P50 CA12832, and 1 S10 RR17858. The authors thank Carlos Arteaga, M.D., for the generous donation of BT474 and HR6 cell lines. We also thank Joseph Roland, Ph.D., Jarrod True, Zoe Yu, M.D., and Carlo Malabanon for animal care assistance.

References

[1] Dean-Colomb W and Esteva FJ (2008). Her2-positive breast cancer: herceptin and beyond. *Eur J Cancer* **44**(18), 2806–2812.

[2] Spector NL and Blackwell KL (2009). Understanding the mechanisms behind trastuzumab therapy for human epidermal growth factor receptor 2-positive breast cancer. *J Clin Oncol* **27**(34), 5838–5847.

[3] Carter P, Presta L, Gorman CM, Ridgway JB, Henner D, Wong WL, Rowland AM, Kotts C, Carver ME, and Shepard HM (1992). Humanization of an anti-p185HER2 antibody for human cancer therapy. *Proc Natl Acad Sci U S A* **89**(10), 4285–4289.

[4] Nahta R and Esteva FJ (2006). HER2 therapy: molecular mechanisms of trastuzumab resistance. *Breast Cancer Res* **8**(6), 215–222.

[5] Ross JS and Fletcher JA (1998). The HER-2/neu oncogene in breast cancer: prognostic factor, predictive factor, and target for therapy. *Stem Cells* **16**(6), 413–428.

[6] Buzdar AU, Ibrahim NK, Francis D, Booser DJ, Thomas ES, Theriault RL, Pusztai L, Green MC, Arun BK, and Giordano SH, et al (2005). Significantly higher pathologic complete remission rate after neoadjuvant therapy with trastuzumab, paclitaxel, and epirubicin chemotherapy: results of a randomized trial in human epidermal growth factor receptor 2-positive operable breast cancer. *J Clin Oncol* **23**(16), 3676–3685.

[7] Piccart-Gebhart MJ, Procter M, Leyland-Jones B, Goldhirsch A, Untch M, Smith I, Gianni L, Baselga J, Bell R, and Jackisch C, et al (2005). Trastuzumab after adjuvant chemotherapy in HER2-positive breast cancer. *N Engl J Med* **353**(16), 1659–1672.

[8] Vogel CL, Cobleigh MA, Tripathy D, Gutheil JC, Harris LN, Fehrenbacher L, Slamon DJ, Murphy M, Novotny WF, and Burchmore M, et al (2002). Efficacy and safety of trastuzumab as a single agent in first-line treatment of HER2-overexpressing metastatic breast cancer. *J Clin Oncol* **20**(3), 719–726.

[9] Hortobagyi GN (2005). Trastuzumab in the treatment of breast cancer. *N Engl J Med* **353**(16), 1734–1736.

[10] Neve RM, Holbro T, and Hynes NE (2002). Distinct roles for phosphoinositide 3-kinase, mitogen-activated protein kinase and p38 MAPK in mediating cell cycle progression of breast cancer cells. *Oncogene* **21**(29), 4567–4576.

[11] Izumi Y, Xu L, di Tomaso E, Fukumura D, and Jain RK (2002). Tumour biology: herceptin acts as an anti-angiogenic cocktail. *Nature* **416**(6878), 279–280.

[12] Klos KS, Zhou X, Lee S, Zhang L, Yang W, Nagata Y, and Yu D (2003). Combined trastuzumab and paclitaxel treatment better inhibits ErbB-2-mediated angiogenesis in breast carcinoma through a more effective inhibition of Akt than either treatment alone. *Cancer* **98**(7), 1377–1385.

[13] Padhani AR, Liu G, Koh DM, Chenevert TL, Thoeny HC, Takahara T, Dzik-Jurasz A, Ross BD, Van Cauteren M, and Collins D, et al (2009). Diffusion-weighted magnetic resonance imaging as a cancer biomarker: consensus and recommendations. *Neoplasia* **11**(2), 102–125.

[14] Loveless ME, Lawson D, Collins M, Nadella MV, Reimer C, Huszar D, Halliday J, Waterton JC, Gore JC, and Yankeelov TE (2012). Comparisons of the efficacy of a Jak1/2 inhibitor (AZD1480) with a VEGF signaling inhibitor (cediranib) and sham treatments in mouse tumors using DCE-MRI, DW-MRI, and histology. *Neoplasia* **14**(1), 54–64.

[15] Anderson AW, Xie J, Pizzonia J, Bronen RA, Spencer DD, and Gore JC (2000). Effects of cell volume fraction changes on apparent diffusion in human cells. *Magn Reson Imaging* **18**(6), 689–695.

[16] Moestue SA, Huuse EM, Lindholm EM, Bofin A, Engebraaten O, Maelandsmo GM, Akslen LA, and Gribbestad IS (2013). Low-molecular contrast agent dynamic contrast-enhanced (DCE)-MRI and diffusion-weighted (DW)-MRI in early assessment of bevacizumab treatment in breast cancer xenografts. *J Magn Reson Imaging* **38**(5), 1043–1053.

[17] Oliver PG, LoBuglio AF, Zhou T, Forero A, Kim H, Zinn KR, Zhai G, Li Y, Lee CH, and Buchsbaum DJ (2012). Effect of anti-DR5 and chemotherapy on basal-like breast cancer. *Breast Cancer Res Treat* **133**(2), 417–426.

[18] Aliu SO, Wilmes LJ, Moasser MM, Hann BC, Li KL, Wang D, and Hylton NM (2009). MRI methods for evaluating the effects of tyrosine kinase inhibitor administration used to enhance chemotherapy efficiency in a breast tumor xenograft model. *J Magn Reson Imaging* **29**(5), 1071–1079.

[19] Jensen LR, Garzon B, Heldahl MG, Bathen TF, Lundgren S, and Gribbestad IS (2011). Diffusion-weighted and dynamic contrast-enhanced MRI in evaluation of early treatment effects during neoadjuvant chemotherapy in breast cancer patients. *J Magn Reson Imaging* **34**(5), 1099–1109.

[20] Li XR, Cheng LQ, Liu M, Zhang YJ, Wang JD, Zhang AL, Song X, Li J, Zheng YQ, and Liu L (2012). DW-MRI ADC values can predict treatment response in patients with locally advanced breast cancer undergoing neoadjuvant chemotherapy. *Med Oncol* **29**(2), 425–431.

[21] Yankeelov TE, Lepage M, Chakravarthy A, Broome EE, Niermann KJ, Kelley MC, Meszoely I, Mayer IA, Herman CR, and McManus K, et al (2007). Integration of quantitative DCE-MRI and ADC mapping to monitor treatment response in human breast cancer: initial results. *Magn Reson Imaging* **25**(1), 1–13.

[22] Yankeelov TE and Gore JC (2009). Dynamic contrast enhanced magnetic resonance imaging in oncology: theory, data acquisition, analysis, and examples. *Curr Med Imaging Rev* **3**(2), 91–107.

[23] Marzola P, Degrassi A, Calderan L, Farace P, Nicolato E, Crescimanno C, Sandri M, Giusti A, Pesenti E, and Terron A, et al (2005). Early antiangiogenic activity of SU11248 evaluated in vivo by dynamic contrast-enhanced magnetic resonance imaging in an experimental model of colon carcinoma. *Clin Cancer Res* **11**(16), 5827–5832.

[24] Haney CR, Fan X, Markiewicz E, Mustafi D, Karczmar GS, and Stadler WM (2013). Monitoring anti-angiogenic therapy in colorectal cancer murine model using dynamic contrast-enhanced MRI: comparing pixel-by-pixel with region of interest analysis. *Technol Cancer Res Treat* **12**(1), 71–78.

[25] Li X, Arlinghaus LR, Ayers GD, Chakravarthy AB, Abramson RG, Abramson VG, Atuegwu N, Farley J, Mayer IA, and Kelley MC, et al (2014). DCE-MRI analysis methods for predicting the response of breast cancer to neoadjuvant chemotherapy: Pilot study findings. *Magn Reson Med* **71**(4), 1592–1602.

[26] Harry VN, Semple SI, Parkin DE, and Gilbert FJ (2010). Use of new imaging techniques to predict tumour response to therapy. *Lancet Oncol* **11** (1), 92–102.

[27] Ritter CA, Perez-Torres M, Rinehart C, Guix M, Dugger T, Engelman JA, and Arteaga CL (2007). Human breast cancer cells selected for resistance to trastuzumab in vivo overexpress epidermal growth factor receptor and ErbB ligands and remain dependent on the ErbB receptor network. *Clin Cancer Res* **13** (16), 4909–4919.

[28] Hurley J, Doliny P, Reis I, Silva O, Gomez-Fernandez C, Velez P, Pauletti G, Powell JE, Pegram MD, and Slamon DJ (2006). Docetaxel, cisplatin, and trastuzumab as primary systemic therapy for human epidermal growth factor receptor 2-positive locally advanced breast cancer. *J Clin Oncol* **24**(12), 1831–1838.

[29] Romond EH, Perez EA, Bryant J, Suman VJ, Geyer Jr CE, Davidson NE, Tan-Chiu E, Martino S, Paik S, and Kaufman PA, et al (2005). Trastuzumab plus adjuvant chemotherapy for operable HER2-positive breast cancer. *N Engl J Med* **353**(16), 1673–1684.

[30] Whisenant JG, McIntyre JO, Peterson TE, Kang H, Sanchez V, Manning HC, Arteaga CL, and Yankeelov TE (2014). Utility of [F]FLT-PET to assess treatment response in Trastuzumab-resistant and Trastuzumab-sensitive HER2-overexpressing human breast cancer xenografts. *Mol Imaging Biol* [Epub ahead of print].

[31] Anderson AW and Gore JC (1994). Analysis and correction of motion artifacts in diffusion weighted imaging. *Magn Reson Med* **32**(3), 379–387.

[32] Mills R (1973). Self-diffusion in normal and heavy water in the range of 1-45 degrees. *J Phys Chem* **77**(5), 685–688.

[33] Kety SS (1951). The theory and applications of the exchange of inert gas at the lungs and tissues. *Pharmacol Rev* **3**(1), 1–41.

[34] Barnes SL, Whisenant JG, Loveless ME, and Yankeelov TE (2012). Practical dynamic contrast enhanced MRI in small animal models of cancer: data acquisition, data analysis, and interpretation. *Pharmaceutics* **4**(3), 442–478.

[35] Loveless ME, Halliday J, Liess C, Xu L, Dortch RD, Whisenant J, Waterton JC, Gore JC, and Yankeelov TE (2012). A quantitative comparison of the influence of individual versus population-derived vascular input functions on dynamic contrast enhanced-MRI in small animals. *Magn Reson Med* **67**(1), 226–236.

[36] Li X, Rooney WD, Varallyay CG, Gahramanov S, Muldoon LL, Goodman JA, Tagge IJ, Selzer AH, Pike MM, and Neuwelt EA, et al (2010). Dynamic-contrast-enhanced-MRI with extravasating contrast reagent: rat cerebral glioma blood volume determination. *J Magn Reson* **206**(2), 190–199.

[37] Donahue KM, Weisskoff RM, Parmelee DJ, Callahan RJ, Wilkinson RA, Mandeville JB, and Rosen BR (1995). Dynamic Gd-DTPA enhanced MRI measurement of tissue cell volume fraction. *Magn Reson Med* **34**(3), 423–432.

[38] Kim H, Folks KD, Guo L, Stockard CR, Fineberg NS, Grizzle WE, George JF, Buchsbaum DJ, Morgan DE, and Zinn KR (2011). DCE-MRI detects early vascular response in breast tumor xenografts following anti-DR5 therapy. *Mol Imaging Biol* **13**(1), 94–103.

[39] Goel S, Duda DG, Xu L, Munn LL, Boucher Y, Fukumura D, and Jain RK (2011). Normalization of the vasculature for treatment of cancer and other diseases. *Physiol Rev* **91**(3), 1071–1121.

[40] Sorace AG, Whisenant JG, McIntyre JO, Sanchez VM, Loveless ME, and Yankeelov TE (2014). Preliminary evidence of a vascular normalization biomarker in trastuzumab-treated HER2+ breast cancer. International Society for Magnetic Resonance in Medicine: 2014; Milan, Italy; 2014.

[41] Jain RK (2005). Normalization of tumor vasculature: an emerging concept in antiangiogenic therapy. *Science* **307**(5706), 58–62.

[42] Heyerdahl H, Roe K, Brevik EM, and Dahle J (2013). Modifications in dynamic contrast-enhanced magnetic resonance imaging parameters after alpha-particle-emitting (2)(2)(7)Th-trastuzumab therapy of HER2-expressing ovarian cancer xenografts. *Int J Radiat Oncol Biol Phys* **87**(1), 153–159.

[43] Fluckiger JU, Loveless ME, Barnes SL, Lepage M, and Yankeelov TE (2013). A diffusion-compensated model for the analysis of DCE-MRI data: theory, simulations and experimental results. *Phys Med Biol* **58**(6), 1983–1998.

[44] Pellerin M, Yankeelov TE, and Lepage M (2007). Incorporating contrast agent diffusion into the analysis of DCE-MRI data. *Magn Reson Med* **58**(6), 1124–1134.